INSTITUTE OF PHYSICS PUBLISHING INVERSE PROBLEMS

Inverse Problems **17** (2001) 293–306 www.iop.org/Journals/ip PII: S0266-5611(01)17290-4

A new SPECT reconstruction algorithm based on the Novikov explicit inversion formula

Leonid A Kunyansky

ACM, Firestone 217-50, California Institute of Technology, Pasadena, CA 91125, USA

E-mail: leonk@acm.caltech.edu

Received 20 September 2000, in final form 12 January 2001

Abstract

We present a new reconstruction algorithm for single-photon emission computed tomography. The algorithm is based on the Novikov explicit inversion formula for the attenuated Radon transform with non-uniform attenuation. Our reconstruction technique can be viewed as a generalization of both the filtered backprojection algorithm and the Tretiak–Metz algorithm. We test the performance of the present algorithm in a variety of numerical experiments. Our numerical examples show that the algorithm is capable of accurate image reconstruction even in the case of strongly non-uniform attenuation coefficient, similar to that occurring in a human thorax.

Introduction

Single-photon emission computed tomography (SPECT) is based on measurements of gamma-rays radiated by trace amounts of a radionuclide injected into a patient. The intensities of the radiation measured by a spatially collimated gamma-camera are related to values of line integrals of the radionuclide distribution, with exponential weights representing attenuation of radiation on its way from a source to the detector. The sought quantity is the radionuclide distribution; it has to be reconstructed numerically from the measured data. The above-mentioned exponential weights are determined by a position-dependent attenuation coefficient; when SPECT is performed in such regions as a human thorax, this dependence cannot be neglected and has to be accounted for by the reconstruction algorithm. In this paper we present a new numerical technique, which, being based on the explicit formula recently discovered by Novikov [1], allows for accurate non-iterative SPECT reconstruction in the presence of arbitrary realistic attenuation.

The variety of existing SPECT algorithms can be split into a family of analytical methods [3–9] and a wide class of iterative techniques (see e.g. [13–19]). Some of the iterative algorithms (such as, for instance, [21–24]) involve evaluation of certain analytic inversion formulae as a part of the method. The advantage of the iterative techniques lies in their flexibility, which allows one to treat realistic mathematical models of the measurements, and, therefore, not only to account for the attenuation of radiation but also to correct for such image

0266-5611/01/020293+14$30.00

degradation factors as collimator blurring and photon scattering. The analytic methods in general, on the other hand, are considerably faster; a wide use of the filtered backprojection algorithm (FBP) in practical x-ray tomography is explained by the efficiency of this analytic technique (see [20] for the description of the FBP algorithm). However, to design an analytic method one needs an explicit inversion formula, which, for realistic mathematical models of the measurements can be difficult to derive—as it is in the case of SPECT.

First analytic methods for the attenuation correction in SPECT were proposed two decades ago by Bellini *et al* [3] and Tretiak and Metz [4]; both algorithms assumed that the attenuation coefficient was constant inside a patient's body and that the cross section of the body was convex. Two more analytic methods were introduced almost a decade later in [5] and [6] (an algorithm similar to [5] was independently developed in [7, 8]). A scheme generalizing all of the above-mentioned approaches has been proposed in [9]; a general analytic approach leading to a variety of reconstruction formulae was given in [10]. Certain extensions to the underlying assumptions of constant attenuation and convex body were treated in [10] and [11]; in the former work an inversion formula was derived for the case when attenuation depends on an observation angle (but is constant for a fixed angle). All of these analytic methods, however, are not applicable for the SPECT of regions with strongly non-uniform attenuation. Creation of the analytic SPECT reconstruction algorithm, operative in the case of arbitrary realistic attenuation coefficient, has become possible only recently, due to the approach developed in [12], and due to the discovery of an explicit inversion formula for the attenuated Radon transform by Novikov [1]. (A simpler derivation of a similar formula was given later by Natterer [2].)

Thus, in this paper we present a new reconstruction algorithm based on the Novikov explicit inversion formula. Since, as we will show, the Novikov formula can be viewed as a generalization of both the Radon inversion formula and the Tretiak–Metz formula, the resulting method contains both the FBP and the Tretiak–Metz scheme (in the cases of zero and constant attenuation, respectively). We test our algorithm using realistic models of attenuation and several activity distribution models. As our numerical experiments show, the use of the explicit inversion scheme allows for accurate non-iterative image reconstruction even within the regions with strongly non-uniform attenuation distributions, similar to the attenuation within a human thorax.

The reconstruction technique we present can be used either directly or as an efficient preconditioner for more complicated reconstruction algorithms capable of correcting not only for effects of non-uniform attenuation but also for other image degradation factors, such as detector blurring and/or photon scattering.

1. Formulation of the problem

Let $f(\boldsymbol{x})$ denote the object radionuclide distribution and $a(\boldsymbol{x})$ be the attenuation coefficient of the body tissue. As shown in figure 1, the detector measures the intensity of radiation $g_\varphi(p)$ emitted in the direction $\boldsymbol{\theta}(\varphi)$ along a line defined by its distance p from the origin; the values of $g_\varphi(p)$ are given by the following equation:

$$g_\varphi(p) \equiv R_{a,\varphi} f = \int_{\mathbb{R}} \exp\left(-D_\varphi a[\boldsymbol{x} + t\boldsymbol{\theta}(\varphi)]\right) f(\boldsymbol{x} + t\boldsymbol{\theta}(\varphi))\, \mathrm{d}t, \tag{1}$$

where the divergent beam transform $D_\varphi a(\boldsymbol{x})$ is defined as follows:

$$D_\varphi a(\boldsymbol{x}) = \int_0^\infty a(\boldsymbol{x} + t\boldsymbol{\theta}(\varphi))\, \mathrm{d}t. \tag{2}$$

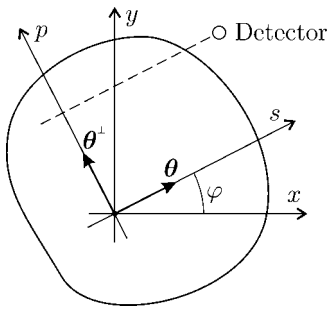

Figure 1. Data acquisition scheme and coordinate systems.

The integral transform given by equation (1) maps function $f(\boldsymbol{x})$ into its projections $g_\varphi(p)$; this transform is usually referred to as the attenuated Radon transform. We will assume that the attenuation coefficient is known (in practice it can be obtained, for example, from transmission measurements as done in [25, 26]). The goal of SPECT is to reconstruct the radionuclide distribution $f(\boldsymbol{x})$ from measured projections $g_\varphi(p)$. The reconstruction algorithm we present is based on the Novikov explicit inversion formula for the attenuated Radon transform.

2. The Novikov explicit inversion formula

In order to simplify presentation we introduce a rotated coordinate system (s, p) with axes parallel to vectors $\boldsymbol{\theta}(\varphi)$ and $\boldsymbol{\theta}^\perp(\varphi)$ (see figure 1) so that

$$s = x\cos\varphi + y\sin\varphi,$$
$$p = -x\sin\varphi + y\cos\varphi.$$

In the new coordinates the integrations defined by equations (1), (2) can be written in a particularly simple form:

$$g_\varphi(p) \equiv \int_{\mathbb{R}} \exp\left(-D^*_\varphi a^*_\varphi(s, p)\right) f^*_\varphi(s, p)\,\mathrm{d}s, \tag{3}$$

$$D^*_\varphi a^*_\varphi(s, p) = \int_s^\infty a^*_\varphi(s', p)\,\mathrm{d}s', \tag{4}$$

where $f^*_\varphi(s, p) = f(\boldsymbol{x}(s, p, \varphi))$, $a^*_\varphi(s, p) = a(\boldsymbol{x}(s, p, \varphi))$ and $D^*_\varphi a^*_\varphi(s, p) = D_\varphi a(\boldsymbol{x}(s, p, \varphi))$.

The (classical) Radon transform R_φ of the attenuation coefficient $a(\boldsymbol{x})$ is defined by the following equation:

$$R_\varphi a(p) = \int_{-\infty}^\infty a^*_\varphi(s', p)\,\mathrm{d}s'. \tag{5}$$

Comparing this expression to (4) one observes that the values of $R_\varphi a(p)$ coincide with limiting values of the divergent beam transform D_φ:

$$R_\varphi a(p) = D^*_\varphi a^*_\varphi(-\infty, p).$$

The goal of the SPECT reconstruction is to recover the radionuclide distribution $f(\boldsymbol{x})$ from projections $g_\varphi(p)$. This problem is equivalent to the inversion of the attenuated Radon transform (1), under the assumption that the attenuation coefficient $a(\boldsymbol{x})$ is known. The explicit inversion formula for this transform has been derived recently by Novikov [1]. We present

the Novikov formula below in a slightly simplified equivalent version that avoids usage of complex-valued integral transforms:

$$f(\boldsymbol{x}) = \frac{1}{4\pi}\left(\frac{\partial}{\partial x_2}B^c(\boldsymbol{x}) - \frac{\partial}{\partial x_1}B^s(\boldsymbol{x})\right), \tag{6}$$

$$\begin{aligned} B^c(\boldsymbol{x}) &= \int_0^{2\pi} \exp\left(D_\varphi a(\boldsymbol{x})\right) m_\varphi(\boldsymbol{x}\cdot\boldsymbol{\theta}^\perp(\varphi))\cos\varphi\,\mathrm{d}\varphi, \\ B^s(\boldsymbol{x}) &= \int_0^{2\pi} \exp\left(D_\varphi a(\boldsymbol{x})\right) m_\varphi(\boldsymbol{x}\cdot\boldsymbol{\theta}^\perp(\varphi))\sin\varphi\,\mathrm{d}\varphi, \end{aligned} \tag{7}$$

where the modified projections $m_\varphi(p)$ are defined as

$$m_\varphi(p) = \mathrm{e}^{-A_\varphi(p)}[h^c_\varphi(p)H(h^c_\varphi(p)\mathrm{e}^{A_\varphi(p)}g_\varphi(p)) + h^s_\varphi(p)H(h^s_\varphi(p)\mathrm{e}^{A_\varphi(p)}g_\varphi(p))], \tag{8}$$

the Hilbert transform H of a function $\psi(u)$ is given by the formula

$$H\psi(u) = \frac{1}{\pi}\mathcal{P}\int_{\mathbb{R}}\frac{\psi(v)}{u-v}\,\mathrm{d}v \tag{9}$$

and

$$\begin{aligned} h^c_\varphi(p) &= \cos\left(HA_\varphi(p)\right), \\ h^s_\varphi(p) &= \sin\left(HA_\varphi(p)\right), \\ A_\varphi(p) &= \tfrac{1}{2}(R_\varphi a)(p). \end{aligned} \tag{10}$$

One can further modify the Novikov formula to a form similar to the Radon or Tretiak–Metz inversion formulae. Namely, note that the differential operator $(-\sin\varphi\frac{\partial}{\partial x_1}, \cos\varphi\frac{\partial}{\partial x_2})$ is equal to $(\boldsymbol{\theta}^\perp(\varphi)\cdot\nabla)$. Application of this operator to a function in (s, p) coordinates is equivalent to differentiation in p, so that formulae (6), (7) can be replaced by the formulae

$$f(\boldsymbol{x}) = \frac{1}{4\pi}\int_0^{2\pi} M_\varphi(\boldsymbol{x}\cdot\boldsymbol{\theta}(\varphi), \boldsymbol{x}\cdot\boldsymbol{\theta}^\perp(\varphi))\,\mathrm{d}\varphi, \tag{11}$$

$$M_\varphi(s, p) = \frac{\partial}{\partial p}[\exp\left(D^*_\varphi a^*_\varphi(s, p)\right)m_\varphi(p)]. \tag{12}$$

3. Relation between the Novikov and Tretiak–Metz inversion formulae

Analysing equations (11), (12) one can easily notice that in the case when attenuation is absent (i.e. $a(\boldsymbol{x}) = 0$) the Novikov inversion formula can be reduced to one of the known inversion formulae for the classical Radon transform (namely, to the formula that involves differentiation and the Hilbert transform of the projections followed by the backprojection step (see [20])). In this section we will show that the Novikov formula also contains the known Tretiak–Metz inversion formula [4] as a particular case.

The formula proposed by Tretiak and Metz allows one to invert the attenuated Radon transform (1) in the case when the body has a convex cross section and the attenuation coefficient $a(\boldsymbol{x})$ is equal to some constant μ inside this cross section. Throughout this section we will assume that these two conditions hold.

Notice first that, under assumptions we have made, the reconstruction problem can be re-formulated into a similar problem with the attenuation $a(\boldsymbol{x}) = \mu$ supported inside a disc; we will assume, without loss of generality, that the radius of the disc is equal to unity. Then, according to the Tretiak–Metz inversion scheme, activity $f(\boldsymbol{x})$ can be reconstructed as a result of the following sequence of operations:

(i) pre-multiplication of projections $g_\varphi(p)$, $p \in [-1, 1]$ by the factor $\mathrm{e}^{\mu\sqrt{1-p^2}}$;

(ii) filtration of the pre-multiplied projections with the filter $w(p)$ given by the formulae

$$\hat{w}(\rho) = \begin{cases} 0, & |\rho| < \mu \\ |\rho|, & |\rho| \geqslant \mu, \end{cases} \qquad \hat{w}(\rho) = (Fw)(\rho) \tag{13}$$

where the Fourier transform F of a function $u(p)$ is defined as

$$\hat{u}(\rho) = Fu = (2\pi)^{-1/2} \int_{\mathbb{R}^1} \mathrm{e}^{-\mathrm{i}\rho p} u(p)\, \mathrm{d}p; \tag{14}$$

(iii) backprojection with the weight $\mathrm{e}^{-\mu(\boldsymbol{x}\cdot\boldsymbol{\theta}(\varphi))}$ of the filtered projections $G_\varphi(p)$ obtained on the previous step:

$$f(\boldsymbol{x}) = \frac{1}{4\pi} \int_0^{2\pi} \mathrm{e}^{-\mu(\boldsymbol{x}\cdot\boldsymbol{\theta}(\varphi))} G_\varphi(\boldsymbol{x}\cdot\boldsymbol{\theta}^\perp(\varphi))\, \mathrm{d}\varphi.$$

One can readily verify that the factor $\mathrm{e}^{A_\varphi(p)}$ in equation (8) under assumptions of this section coincides with the function $\mathrm{e}^{\mu\sqrt{1-p^2}}$ utilized in the first step of the Tretiak–Metz scheme. It is also easy to see that the combination of the factors $\mathrm{e}^{-A_\varphi(p)}$ from equation (8) and $\exp(D_\varphi^* a_\varphi^*(s, p))$ from equation (12) does not depend on p, so that (12) can be re-written as

$$f(\boldsymbol{x}) = \frac{1}{4\pi} \int_0^{2\pi} \mathrm{e}^{-\mu(\boldsymbol{x}\cdot\boldsymbol{\theta}(\varphi))} \left(\frac{\partial}{\partial p} m_\varphi\right)(\boldsymbol{x}\cdot\boldsymbol{\theta}^\perp(\varphi))\, \mathrm{d}\varphi.$$

In other words, the last step of the Novikov inversion scheme coincides with the last step of the Tretiak–Metz method.

In order to prove the equivalence of the two inversion formulae under the assumptions of this section, one has to show that the Novikov filtration operator Nu defined according to equations (8), (12) by the formulae

$$Nu(p) = \frac{\partial}{\partial p} \Upsilon u(p), \tag{15}$$

$$\Upsilon u(p) = h_\varphi^c(p) H(h_\varphi^c(p) u(p)) + h_\varphi^s(p) H(h_\varphi^s(p) u(p)), \tag{16}$$

with functions $h_\varphi^c(p)$ and $h_\varphi^s(p)$ given by (10), is equivalent to the filtration with the filter $w(p)$ (see equation (13)) used in the Tretiak–Metz scheme. Let us notice first that the function $A_\varphi(p)$ and its Hilbert transform $HA_\varphi(p)$ in equation (10) under our assumptions can be evaluated for values of p in the interval $[-1, 1]$ as follows:

$$A_\varphi(p) = \begin{cases} \mu\sqrt{1-p^2}, & |p| \leqslant 1 \\ 0, & |p| > 1, \end{cases} \tag{17}$$

$$HA_\varphi(p) = \mu p; \tag{18}$$

for the proof of (18) see the appendix. Now the operator $\Upsilon u(p)$ can be represented as follows:

$$\begin{aligned} \Upsilon u(p) &= \cos(\mu p) H(\cos(\mu p) u(p)) + \sin(\mu p) H(\sin(\mu p) u(p)) \\ &= \tfrac{1}{2}[\mathrm{e}^{\mathrm{i}\mu p} H(\mathrm{e}^{-\mathrm{i}\mu p} u(p)) + \mathrm{e}^{-\mathrm{i}\mu p} H(\mathrm{e}^{\mathrm{i}\mu p} u(p))]. \end{aligned}$$

Taking into account that multiplication by the factor $\mathrm{e}^{\mathrm{i}\mu p}$ shifts the Fourier transform $\hat{u}(\rho)$ of the function $u(p)$ by μ, and that the Hilbert transform H multiplies $\hat{u}(\rho)$ by $(-\mathrm{i}\,\mathrm{sign}\rho)$, one sees that the Fourier transformant $\widehat{\Upsilon u}(\rho)$ of the function $\Upsilon u(p)$ is given by

$$\widehat{\Upsilon u}(\rho) = -\mathrm{i}(\hat{u}^+(\rho) - \hat{u}^-(\rho)), \tag{19}$$

where

$$\hat{u}^+(\rho) = \begin{cases} \hat{u}(\rho), & \rho \geqslant \mu \\ 0, & \rho < \mu, \end{cases} \qquad \hat{u}^-(\rho) = \begin{cases} \hat{u}(\rho), & \rho \leqslant -\mu \\ 0, & \rho > -\mu. \end{cases} \tag{20}$$

Equation (19) allows one to evaluate the Fourier transform $\widehat{Nu}(\rho)$ of $Nu(p)$; namely, since differentiation $\partial/\partial p$ is equivalent to multiplication of the Fourier transform of a function by the factor $i\rho$, the transformant $\widehat{Nu}(\rho)$ is given by the following expression:

$$\widehat{Nu}(\rho) = |\rho|(\hat{u}^+(\rho) + \hat{u}^-(\rho)).$$

Comparing the above equation with the expression for the Tretiak–Metz filter (13) we see that, under the assumptions of this section, the two formulae are equivalent, i.e. they represent the same left inverse operator.

4. Reconstruction algorithm

According to equations (8)–(12) one can reconstruct radionuclide distribution $f(\boldsymbol{x})$ from the projections $g_\varphi(p)$ by:

(i) evaluating the divergent beam transform $D_\varphi a(\boldsymbol{x})$ and the Radon transform $R_\varphi a(p)$,
(ii) evaluating the Hilbert transformant of $A_\varphi(p)$,
(iii) computing modifying projections $m_\varphi(p)$ (see equation (8)),
(iv) differentiating the product $\exp(D^*_\varphi a^*_\varphi(s, p))m_\varphi(p)$ in p (see equation (12)) and
(v) backprojecting the result of the differentiation $M_\varphi(s, p)$ (see equation (11)).

The reconstruction algorithm we present follows the structure of the inversion formula. We assume that the data $g_\varphi(p)$ are discretized uniformly in both radial (p) and angular (φ) variables, i.e. values of $g_{\varphi_i}(p_j)$, $i = 1, 2, \ldots, n_\varphi$, $j = 1, 2, \ldots, n_\mathrm{p}$, are given, where n_φ is the number of projections, n_p is the discretization size of each projection, $\varphi_i = 2\pi(i-1)/n_\varphi$, $p_j = -R + \Delta p(j-1)$, $\Delta p = 2R/(n_\mathrm{p} - 1)$, and where R is the radius of the image support. It is also assumed that the attenuation coefficient $a(\boldsymbol{x})$ is known and given by its values on the same Cartesian grid on which the image will be reconstructed.

The discretization of the projections suggests natural discretization for most of the involved functions and integral transforms. In particular, we will approximate backprojection (11) by the following finite sum:

$$f(\boldsymbol{x}) \approx \frac{2\pi}{n_\varphi} \sum_{i=1}^{n_\varphi} M_{\varphi_i}(\boldsymbol{x}\cdot\boldsymbol{\theta}(\varphi_i), \boldsymbol{x}\cdot\boldsymbol{\theta}^\perp(\varphi_i)), \qquad i = 1, 2, \ldots, n_\varphi. \tag{21}$$

Accordingly, we will have to compute values of all other quantities used in the algorithm corresponding to the values φ_i, $i = 1, 2, \ldots, n_\varphi$.

4.1. Divergent beam transform

For each given angle φ_i we evaluate the divergent beam transform $D^*_\varphi a^*_\varphi(s, p)$ using integration in the (s, p) coordinate system, as given by equation (4), for each value of p_j, $j = 1, 2, \ldots, n_\mathrm{p}$. The integrals are computed using the trapezoidal rule with the step $\Delta s = \Delta p$. Since the object's cross section has a finite support, the integration domain is finite (i.e. $[s, \sqrt{R^2 - p^2}]$). Moreover, use of the trapezoidal rule leads to the following recurrence relation:

$$D^*_\varphi a^*_\varphi(-R + k\Delta s, p) \approx D^*_\varphi a^*_\varphi(-R + (k+1)\Delta s, p) + \frac{\Delta s}{2}[a^*_\varphi(-R + k\Delta s, p) + a^*_\varphi(-R + (k+1)\Delta s, p)].$$

This recurrence relation allows us to obtain n_p^2 values $D^*_{\varphi_i} a^*_{\varphi_i}(s_k, p_j)$, $j, k = 1, 2, \ldots, n_\mathrm{p}$, on the (s, p) grid in $\mathcal{O}(n_\mathrm{p}^2)$ operations, where $s_k = -R + \Delta s(k-1)$. Since the values of the attenuation coefficient $a(\boldsymbol{x})$ are given at the nodes of the Cartesian grid in (x, y) coordinates,

the bilinear interpolation is used to obtain values of $a^*_\varphi(s, p) = a(\boldsymbol{x}(s, p, \varphi))$ necessary for the integration in (s, p) coordinates.

Due to the equation (5), after the divergent transform is computed for the current value of φ_i, we automatically obtain values of $A_{\varphi_i}(p_j)$, $j = 1, 2, \ldots, n_\mathrm{p}$ (see equation (10)); they are equal simply to $\frac{1}{2} D^*_{\varphi_i} a^*_{\varphi_i}(s_1, p_j)$.

4.2. Hilbert transform

Having computed $A_{\varphi_i}(p_j)$, $j = 1, 2, \ldots, n_\mathrm{p}$, for a given angle φ_i, one can evaluate the Hilbert transform of $A_{\varphi_i}(p)$ as required by (10). The Hilbert transform can be viewed as a convolution with the kernel $1/(\pi p)$; we approximate such a convolution by a discrete convolution with the kernel represented by the following sequence of values K_j, $j = -n_\mathrm{p}, \ldots, n_\mathrm{p}$:

$$K_j = \frac{1}{\pi}\left[j \ln\left(1 - \frac{1}{j^2}\right) + \ln\frac{j+1}{j-1}\right], \qquad j = 2, \ldots, n_\mathrm{p}$$
$$K_1 = \frac{2}{\pi}\ln 2, \qquad K_0 = 0,$$
$$K_{-j} = -K_j, \qquad j = -n_\mathrm{p}, \ldots, 1.$$

This sequence can be viewed as values of the approximate kernel $1/(\pi p) * \eta(p)$ at the points $p = p_j$, where the roof-top function $\eta(p)$ is defined as

$$\eta(p) = \begin{cases} \dfrac{1}{\Delta p}(p+1), & -\Delta p \leqslant p \leqslant 0, \\ \dfrac{1}{\Delta p}(1-p), & 0 \leqslant p \leqslant \Delta p, \\ 0, & |p| > \Delta p. \end{cases}$$

The use of such a discrete kernel is equivalent to performing a linear interpolation of a function between values p_j followed by exact convolution with the kernel $1/(\pi p)$. The convolution of the kernel $1/(\pi p)$ with the function $\eta(p)$ can also be viewed as a low-frequency filtration performed with a filter equal to the Fourier transformant $\hat{\eta}(\rho)$ of $\eta(\rho)$:

$$\hat{\eta}(\rho) = \left(\frac{\sin(\pi\rho/\rho^{\mathrm{Nyquist}})}{\pi\rho/\rho^{\mathrm{Nyquist}}}\right)^2$$

where ρ^{Nyquist} is the Nyquist frequency of the discretization.

As numerical examples of section 5 show, the above-mentioned low-frequency filtration implicit in our implementation of the Hilbert transform is sufficient to provide stable reconstruction in the case of low noise-to-signal ratio. When the noise level is high, however, we employ an additional low-frequency filter $\hat{W}(\rho)$ given by

$$\hat{W}(\rho) = \begin{cases} \frac{1}{2}(1 + \cos(\pi\rho/\rho^{\text{cut-off}})), & |\rho| \leqslant \rho^{\text{cut-off}} \\ 0, & |\rho| > \rho^{\text{cut-off}}, \end{cases} \tag{22}$$

where $\rho^{\text{cut-off}}$ is the cut-off frequency, $\rho^{\text{cut-off}} \leqslant \rho^{\mathrm{Nyquist}}$.

Thus, the Hilbert transform of a function is evaluated by zero padding the function (represented by n_p samples) to $2n_\mathrm{p}$ samples, followed by the discrete convolution with the approximate kernel $\{K_j\}$ performed in the frequency domain using the fast Fourier transform algorithm (FFT). In addition, when necessary, the Fourier spectrum of the signal is also multiplied by $\hat{W}(\rho)$ in this step of computations. We utilize this implementation of the Hilbert transform throughout the algorithm to compute values of the functions $h^c_{\varphi_i}(p_j)$ and $h^s_{\varphi_i}(p_j)$, and to evaluate the modified projections $m_{\varphi_i}(p_j)$, see equation (8).

4.3. Differentiation and backprojection

The differentiation of the product $\exp[D_\varphi^* a_\varphi^*(s, p)]m_\varphi(p)$, as required by equation (12) can be easily performed using finite differences. Indeed, as a result of the previous steps of the algorithm the values of this product are known at the nodes of Cartesian grid in (s, p) variables. Various finite-difference expressions can be used here to approximate the derivatives; all results presented in section 5 were obtained using the following formula [27]:

$$u'(p) \approx \frac{1}{12\Delta p}[8(u(p+2\Delta p) - u(p-2\Delta p)) - u(p+\Delta p) - u(p-\Delta p)].$$

As a result of the differentiation step we obtain values of $M_{\varphi_i}(s_k, p_j)$ at the nodes of the (s, p) grid.

The final step of the algorithm consists in backprojection of the previously computed quantity $M_{\varphi_i}(s, p)$, as required by equation (21), to reconstruct the image $f(\boldsymbol{x})$. In this step we utilize, again, the bilinear interpolation, in order to obtain values $M_{\varphi_i}(\boldsymbol{x}\cdot\boldsymbol{\theta}(\varphi_i), \boldsymbol{x}\cdot\boldsymbol{\theta}^\perp(\varphi_i))$ from known values $M_{\varphi_i}(s_k, p_j)$.

This completes the description of our algorithm. Assuming that the number of projections n_φ, the number of samples n_p and the size n of the reconstruction grid are of the same order, i.e. $n_\varphi \sim n_\mathrm{p} \sim n$, one can easily conclude that the number of operations required by the present reconstruction method is equal to $\mathcal{O}(n^3)$.

5. Numerical examples

5.1. Phantoms

The goal of this section is to demonstrate the ability of the present technique to reconstruct images in cases of realistic attenuation coefficients, and to test the sensitivity of the algorithm to noise in the data. To this end the following model radionuclide distributions will be utilized. The first activity phantom is described by the characteristic function $\chi_{\mathrm{ell}}(\boldsymbol{x})$ of an ellipse with the axis length ratio 3 : 4, see figure 2(*a*); this object will be used to test the ability of the algorithm to reconstruct slowly varying spatial distributions. We will refer to this function as phantom 1. The second activity model we use, phantom 2, consists of a set of bell-shaped functions, see figure 2(*b*). Some of these test objects are defined by characteristic functions of circles, while the others are given by functions $u_i(\boldsymbol{x}, \boldsymbol{x}_i, r_i)$ of the following form:

$$u_i(\boldsymbol{x}, \boldsymbol{x}_i, r_i) = \begin{cases} (1 - (\boldsymbol{x}-\boldsymbol{x}_i)^2/{r_i}^2)^2, & r \leqslant r_i \\ 0, & r > r_i. \end{cases}$$

This phantom 2 will be used to probe the ability of the algorithm to reproduce smaller details and fast-varying or discontinuous distributions.

To model the attenuation coefficient we use the following functions. When comparing the performance of the present algorithm to our version of the Tretiak–Metz scheme, the attenuation is modelled by the characteristic function $\chi_{\mathrm{ell}}(\boldsymbol{x})$ of the ellipse (shown in figure 2(*a*)) multiplied by a certain constant μ. The value of this constant is chosen so that the optical lengths of the axes are equal to 3.375 and 4.5. (The optical length is a dimensionless quantity equal to an integral of the attenuation coefficient along a path—or, in this case, to the product of the axis length and μ.)

To simulate a realistic strongly non-uniform attenuation coefficient we utilize the phantom used in [22]. This model imitates an attenuation distribution across a section of a human thorax; it consists of an ellipsoidal body with axes of length 22.5 and 30 cm, which, in turn, contains two smaller ellipsoidal regions with axes of length 10 and 8.8 cm, and two circular regions

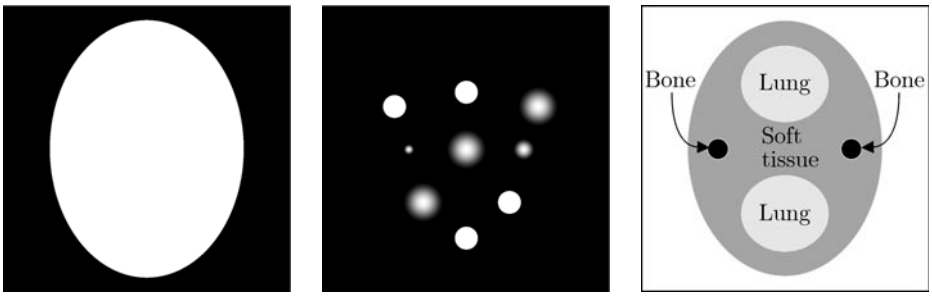

(*a*) (*b*) (*c*)

Figure 2. Model distributions: (*a*) activity phantom 1; (*b*) activity phantom 2; (*c*) attenuation phantom from [22].

of diameter 2.5 cm, see figure 2(*c*). The smaller ellipsoidal regions simulate lungs, while the circular regions correspond to bones; attenuation is equal to 0.01 cm^{-1} within 'lungs' and to 0.17 cm^{-1} within 'bones'. Attenuation within the rest of the large ellipse is equal to 0.15 cm^{-1}.

The size of the image grid and the dimensions $(n_\varphi, n_\mathrm{p})$ of data sets are among the most important factors determining quality of tomography reconstruction. In our numerical experiments all images were computed on a 129×129 grid; the same discretization step was used for projection sampling (i.e. n_p was equal to 129). The number of projections n_φ was chosen taking into account the following considerations. The (approximately) optimal relation between the values n_φ and n_p in the case of transmission tomography is $n_\varphi/n_\mathrm{p} \approx \pi/2$ (see e.g. [20]). Unlike transmission tomography, where projections are measured in the angular range $[0, \pi]$, SPECT measurements cover the range of angles from 0 to 2π. One may assume, therefore, that in SPECT the optimal ratio of n_φ and n_p is given by

$$n_\varphi/n_\mathrm{p} \approx \pi.$$

In order to satisfy this requirement 400 projections were used in all simulations presented below.

Finally, notice that images presented below were drawn using a linear grey scale, in such a way that the dark grey colour represents zero (or negative values, if any) and the white colour corresponds to the maximum value of the *reconstructed* function.

5.2. Reconstruction in the case of constant attenuation

In this section we test the performance of the algorithm based on the Novikov inversion formula in the case of constant attenuation. A model attenuation distribution we use is equal to a constant inside the ellipse shown in figure 2 (see the previous section for the details). Figure 3 shows reconstructions of phantoms 1 and 2 produced by the present algorithm. The computed images are very close to the originals in this simple case. Our version of the Tretiak–Metz algorithm also yields good results in this test; the resulting images practically coincide with those shown in figure 3.

5.3. Reconstruction in the case of non-uniform attenuation

The images presented in this section were reconstructed from attenuated measurements corresponding to a strongly non-uniform attenuation coefficient as modelled by the phantom

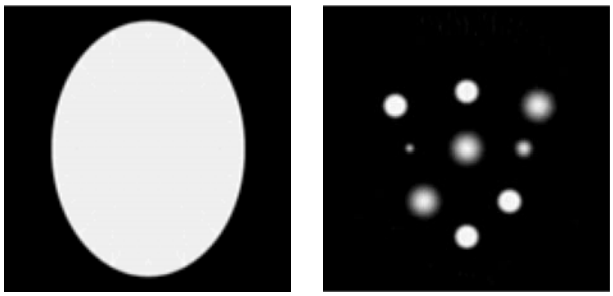

(*a*) (*b*)

Figure 3. Constant-attenuation case: (*a*) reconstruction of the activity phantom 1; (*b*) reconstruction of the activity phantom 2.

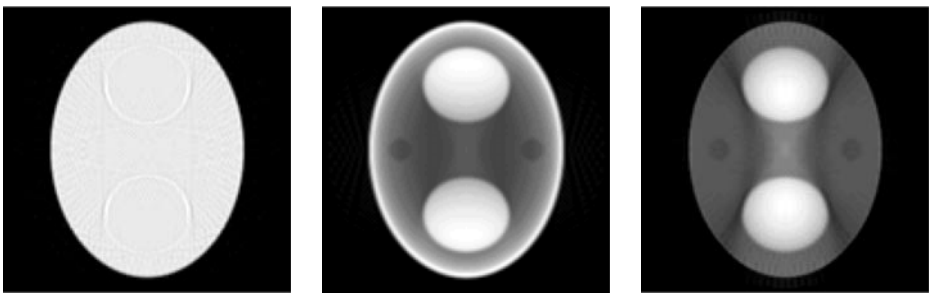

(*a*) (*b*) (*c*)

Figure 4. Reconstructions of the activity phantom 1 in the presence of strong non-uniform attenuation: (*a*) present method; (*b*) FBP algorithm; (*c*) Tretiak–Metz scheme.

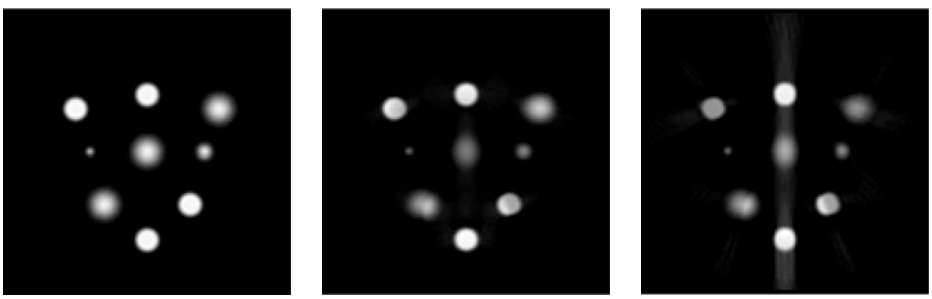

(*a*) (*b*) (*c*)

Figure 5. Reconstructions of the activity phantom 2 in the presence of strong non-uniform attenuation: (*a*) present method; (*b*) FBP algorithm; (*c*) Tretiak–Metz scheme.

utilized in [22] (see figure 2(*c*) and the description given in section 5.1). We experimented with both activity phantoms 1 and 2; the results are shown in figures 4 and 5 respectively.

Figures 4(*a*) and 5(*a*) show images computed using the Novikov formula. Images obtained without any attenuation correction (using the FBP algorithm) are presented in figures 4(*b*) and 5(*b*). Finally, figures 4(*c*) and 5(*c*) demonstrate results of reconstruction obtained from the Tretiak–Metz algorithm with constant attenuation coefficient μ set to the value of 0.15 cm^{-1} (the chosen value of μ is equal to the attenuation coefficient inside the large grey elliptical

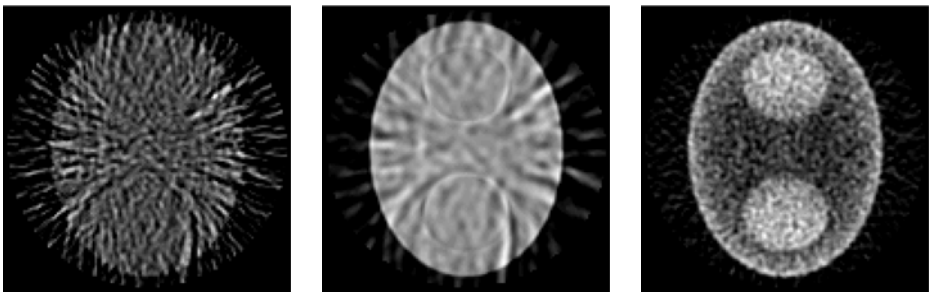

(*a*) (*b*) (*c*)

Figure 6. Reconstructions of the activity phantom 1 from noisy data in the presence of strong non-uniform attenuation: (*a*) present method; (*b*) present method with low-frequency filtration; (*c*) un-apodized FBP algorithm.

region shown in figure 2(*c*)). The versions of the FBP and Tretiak–Metz algorithms we used here were not apodized, i.e. filtration steps of these methods were performed by computing the Fourier transform of the (pre-multiplied) projections using the FFT, by multiplying the transformants by the filters $|\rho|$ or $\hat{w}(\rho)$ (see equation (13)) respectively and by computing the inverse FFT.

The computational examples of this section show that the reconstructions obtained without proper correction for non-uniform attenuation differ significantly from the originals (cf figures 2(*a*), (*b*)); the present algorithm, on the other hand, yields images which are quite close to the corresponding phantoms used in the simulations.

5.4. Reconstruction from noisy data

We conclude our presentation demonstrating the results of the reconstructions from noisy data, obtained in the case of strong non-uniform attenuation. The same model functions are used as in the previous section; in order to simulate quantum noise in the data, the following procedure was implemented on each data set used.

- The projections were scaled (multiplied by a constant factor) so that the maximum 'measured' value in the data set was equal to 50;
- each point value in the data set was then replaced by a random realization of a Poisson variate with a mean equal to that value.

The L^2 intensity of the thus-generated noise was equal to 17.5% for the projections corresponding to phantom 1, and to 21.9% for the projections resulting from phantom 2.

The sets of images presented in figures 6 and 7 correspond to the activity phantoms 1 and 2 respectively; the projections were generated using the non-uniform attenuation map shown in figure 2(*c*). The first images (figures 6(*a*) and 7(*a*)) in these two sets were computed using the present algorithm without additional filtration. Images in figures 6(*b*) and 7(*b*) were produced by our method with application of the low-frequency filter $\hat{W}(\rho)$ given by equation (22) with $\rho^{\mathrm{cut-off}} = \rho^{\mathrm{Nyquist}}/2$; this additional filtration was used in order to reduce the magnitude of the noise-related artifacts. Finally, the last images (figures 6(*c*) and 7(*c*)) in both sets were reconstructed using the un-apodized FBP algorithm.

Analysing images presented in figures 6 and 7 one can observe that:

- the additional low-frequency filtration reduces oscillations in the reconstructed images but results in certain loss of fine details (cf figures 7(*a*) and 7(*b*)),

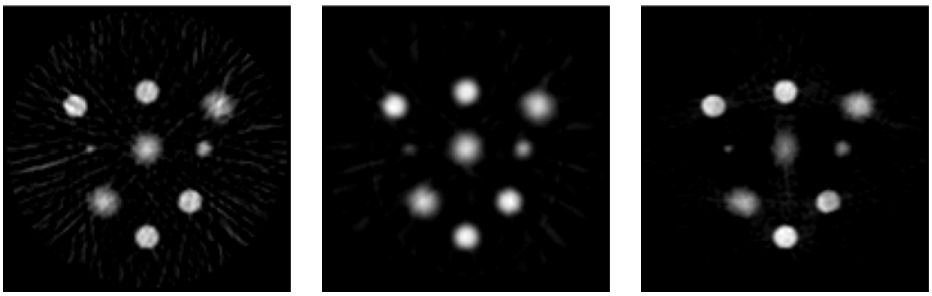

(*a*) (*b*) (*c*)

Figure 7. Reconstructions of the activity phantom 2 from noisy data in the presence of strong non-uniform attenuation: (*a*) present method; (*b*) present method with low-frequency filtration; (*c*) un-apodized FBP algorithm.

- the un-apodized algorithm based on the Novikov explicit reconstruction formula is more sensitive to noise in data than the (un-apodized) FBP algorithm (compare figures 6(*a*) against (*c*), and 7(*a*) against (*c*)) and
- reconstructions obtained from the FBP algorithm (although less noisy) are inaccurate—as a result of strong non-uniform attenuation of radiation on its way from sources to the detector.

To summarize, our numerical results show that the present method based on the Novikov explicit formula can indeed be used for the accurate inversion of the attenuated Radon transform in the case of arbitrary realistic attenuation coefficient and moderately noisy data. However, the possibility of application of the present or similar algorithms to real data (usually containing an intensive noise component) requires further investigation (certain heuristic approaches increasing robustness of the algorithm are discussed in [30]).

Acknowledgments

After this paper had been completed, Professor F Natterer informed us that he independently implemented a similar algorithm; we express our gratitude to F Natterer for the information. The author is also indebted to Professor P Kuchment for encouragement and helpful suggestions, and to Dr W G Hawkins for numerous discussions. Finally, the author would like to thank the reviewers of the manuscript for helpful comments.

Appendix

In this appendix we show that the Hilbert transform $HA_\varphi(p)$ of the function $A_\varphi(p)$ given by equation (18) is equal to μp for $|p| < 1$. Thus, we have to evaluate the following integral (understood in the principal value sense):

$$\begin{aligned} HA_\varphi(p) &= \frac{1}{\pi}\mathcal{P}\int_{-1}^{1}\frac{\mu\sqrt{1-v^2}}{p-v}\,\mathrm{d}v \\ &= \frac{\mu}{\pi}\lim_{\varepsilon\to 0}[F_\mathrm{p}(p-\varepsilon) - F_\mathrm{p}(-1) + F_\mathrm{p}(1) - F_\mathrm{p}(p+\varepsilon)], \end{aligned} \tag{A.1}$$

where the primitive $F_\mathrm{p}(v)$ satisfies the equation

$$\frac{\mathrm{d}}{\mathrm{d}v}F_\mathrm{p}(v) = \frac{\sqrt{1-v^2}}{p-v}.$$

The explicit expression for $F_{\mathrm{p}}(v)$ can be derived by using formulae 2.261, 2.266, 2.267 of [28], and by taking into account the relation between the inverse hyperbolic tangent and cotangent 4.6.7 of [29]:

$$\begin{aligned} F_{\mathrm{p}}(v) &= -\sqrt{1-v^2} + p \arcsin v + \frac{1}{\sqrt{1-p^2}} \operatorname{arccoth} u(p, v), \\ u(p, v) &= \frac{1 - pv}{\sqrt{1-p^2}\sqrt{1-v^2}}, \qquad |p| < 1. \end{aligned} \tag{A.2}$$

Substituting (A.2) into equation (A.1) we obtain

$$\begin{aligned} H A_{\varphi}(p) &= \frac{\mu}{\pi} \left[\pi p + \frac{1}{\sqrt{1-p^2}} \lim_{\varepsilon \to 0} (\operatorname{arccoth} u(p, p-\varepsilon) - \operatorname{arccoth} u(p, p+\varepsilon)) \right] \\ &= \mu p + \frac{\mu}{\sqrt{1-p^2}} \lim_{\varepsilon \to 0} (\operatorname{arccoth} u(p, p-\varepsilon) - \operatorname{arccoth} u(p, p+\varepsilon)). \end{aligned} \tag{A.3}$$

Notice that function $u(p, v)$ is at least twice differentiable on the open unit square $]-1, 1[\times]-1, 1[$; for a fixed p function $u(p, v)$ achieves its minimum at the point $v = p$. Therefore, in a small neighbourhood of p this function admits the following expansion:

$$u(p, p+\varepsilon) = 1 + \frac{1}{2} \frac{\partial^2}{\partial v^2} u(p, p) \varepsilon^2 + \mathcal{O}(\varepsilon^3).$$

Combining the above expansion with the equivalent representation for the hyperbolic cotangent

$$\operatorname{arccoth} x = \frac{1}{2} \ln \frac{x+1}{x-1}$$

one can show that the limit in (A.3) is equal to zero, which yields the desired result

$$H A_{\varphi}(p) = \mu p, \qquad |p| < 1.$$

References

[1] Novikov R 2000 An inversion formula for the attenuated x-ray transformation *Preprint* (*Ark. Mat.* to be published)

[2] Natterer F 2001 Inversion of the attenuated Radon transform *Inverse Problems* **17** 113–9

[3] Bellini S, Piacentini M, Cafforio C and Rocca F 1979 Compensation of tissue absorption in emission tomography *IEEE Trans. Acoust. Speech Signal Process.* **27** 213–8

[4] Tretiak O J and Metz C 1980 The exponential Radon transform *SIAM. J. Appl. Math.* **39** 341–54

[5] Hawkins W G, Leichner P K and Yang N C 1988 The circular harmonic transform for SPECT reconstruction and boundary conditions on the Fourier transform of the sinogram *IEEE Trans. Med. Imaging* **7** 135–48

[6] Inouye T, Kose K and Hasegawa A 1989 Image reconstruction algorithm for single-photon-emission computed tomography with uniform attenuation *Phys. Med. Biol.* **34** 299–304

[7] Shneiberg I Ya 1991 The exponential Radon transform *Dokl. Akad. Nauk* **320** 567–71 (in Russian) (Engl. transl. 1992 *Sov. Math.–Dokl.* **44** 512–6)

[8] Shneiberg I, Ponomarev I, Dmitrichenko V and Kalashnikov S 1994 On a new reconstruction algorithm in emission tomography *Applied Problems of Radon Transform* ed S Gindikin (*AMS Transl. Ser. 2* **162** 247–55)

[9] Metz C E and Pan X 1995 A unified analysis of exact methods of inverting the 2D exponential Radon transform, with implications for noise control in SPECT *IEEE Trans. Med. Imaging* **14** 643–58

[10] Kuchment P and Shneiberg I 1994 Some inversion formulas in the single photon emission tomography *Appl. Anal.* **53** 221–31

[11] Kuchment P 1994 On inversion and range characterization of one transform arising in emission tomography *Proc. Conf. on 75 Years of the Radon Transform* (Hong Kong: International) pp 240–8

[12] Arbuzov E V, Bukhgeim A L and Kazantsev S G 1998 Two-dimensional tomography problems and the theory of A-analytic functions *Siberian Adv. Math.* **8** 1–20

[13] Veklerov E and Llacer J 1988 MLE reconstruction of a brain phantom using a Monte Carlo transition matrix and a statistical stopping rule *IEEE Trans. Nucl. Sci.* **35** 603–7

[14] Hebert T, Leahy R and Singh M 1988 Fast MLE for SPECT using an intermediate polar representation and a stopping criterion *IEEE Trans. Nucl. Sci.* **35** 615–9
[15] Tsui B M W, Hu H-B, Gilland D R and Gullberg G T 1988 Implementation of simultaneous attenuation and detector response correction in SPECT *IEEE Trans. Nucl. Sci.* **35** 778–83
[16] Liang Z and Hart H 1988 Bayesian reconstruction in emission computerized tomography *IEEE Trans. Nucl. Sci.* **35** 788–92
[17] Tsui B M W, Gullberg G T, Edgerton E R, Ballard J G, Perry J R, McCartney W H and Berg J 1989 Correction of nonuniform attenuation in cardiac SPECT imaging *J. Nucl. Med.* **30** 497–507
[18] Zeng G L, Gulberg G T, Tsui B M W and Terry J A 1991 Three-dimensional iterative reconstruction algorithms with attenuation and geometric point response correction *IEEE Trans. Nucl. Sci.* **38** 693–702
[19] Lalush D S and Tsui B M W 1994 Improving the convergence of iterative backprojection algorithms *Med. Phys.* **21** 1283–6
[20] Natterer F 1986 *The Mathematics of Computerized Tomography* (New York: Wiley)
[21] Chang L T 1978 A method for attenuation correction in radionuclide computed tomography *IEEE Trans. Nucl. Sci.* **25** 638–43
[22] Manglos S H, Jaszczak R I, Floyd C E, Hahn L J, Greer K L and Coleman R E 1987 Nonisotropic attenuation in SPECT: phantom tests of quantitative effects and compensation techniques *J. Nucl. Med.* **28** 1584–91
[23] Morozumi T, Nakajima M, Ogawa K and Yuta S 1984 Attenuation correction methods using the information of attenuation distribution for single photon emission CT *Med. Imaging Technol.* **2** 20–9
[24] Kunyansky L A 1992 Generalized and attenuated Radon Transforms: restorative approach to the numerical inversion *Inverse Problems* **8** 809–19
[25] Blankespoor S C, Wu X, Kalki K, Brown J K, Tany H R, Cann C E and Hasegawa B H 1996 Attenuation correction of SPECT using x-ray CT on an emission transmission CT system: myocardial perfusion assessment *IEEE Trans. Nucl. Sci.* **43** 2263–74
[26] Kimiaei S and Larson S A 1996 Simultaneous SPECT and CT with an opposed dual head gamma camera system and conventional parallel hole collimators *IEEE Trans. Nucl. Sci.* **43** 2239–43
[27] Korn G A and Korn T M 1961 *Mathematical Handbook for Scientists and Engineers; Definitions, Theorems, and Formulas for Reference and Review* (New York: McGraw-Hill)
[28] Gradshtein I S and Ryzhik I M 1980 *Table of Integrals, Series, and Products* (New York: Academic)
[29] Abramowitz M and Stegun I A 1972 *Handbook of Mathematical Functions* (New York: Dover)
[30] Kunyansky L 2000 A new SPECT reconstruction algorithm based on the Novikov's explicit inversion formula *Mathematical Physics Preprint Archive* manuscript 00-342